Physical sources of sound in laminar and turbulent jets

S. Sinayoko[*]

Institute of Sound and Vibration Research, University of Southampton

A. Agarwal[†]

Department of Engineering, University of Cambridge

R. D. Sandberg[‡]

School of Engineering Sciences, University of Southampton

An algorithm to compute the physical sources of sound in a jet is introduced. The algorithm is based on spatio-temporal filtering of the flow field and is applicable to multi-frequency sources. It is first applied to an axisymmetric laminar jet and the resulting sources are validated successfully. It is shown that the dominant source mechanism is the "shear-noise" term. The algorithm is also applied to a fully turbulent jet obtained by Direct Numerical Simulation. The sound sources are computed for the axisymmetric mode over a broad range of frequencies. Various physical sources of sound, including monopoles, wavepackets, and vortex pairings are identified.

Introduction

A key problem in identifying the noise sources in jets is that they get swamped by the much larger hydrodynamic fluctuations and become inaccessible. Equivalent sound sources can however be computed by means of an acoustic analogy: the sound field generated by these sources is identical to the sound radiating in the far field within the original flow.[1–3] However, two different noise sources can generate the same sound field. It is therefore problematic to base our understanding of the noise generation on these equivalent sound sources: the sound producing mechanism for the equivalent sound sources may be completely different than the one occurring in the physical flow field.

In an acoustic analogy, the flow is linearised around a particular base flow, and the associated sound sources are computed. These sources radiate sound within the chosen base flow, not the physical flow. Possible choices for the base flow include a quiescent medium,[1] a parallel flow[2] and a time-averaged base flow.[3,4] These base flows are all significantly different from the actual jet, therefore the sound sources are bound to be contaminated by propagation effects and hydrodynamic-field sources.

Goldstein[5] proposed an alternative approach, in which the base flow includes almost all the non-radiating part of the flow field. Because the base flow is so close to the physical flow field and the field linearised about the base flow contains only the radiating field, the associated sources should be close to the true sources of sound. Building on Goldstein's work, Sinayoko *et al.*[6] presented a simplified expression for the sound sources. They showed that it is possible to separate the radiating components from the non-radiating components in a laminar jet, and that the sound sources can be computed.

Using this new approach could help answer some of the outstanding questions on noise generation in subsonic jets. For example, what role, if any, do large coherent structures play in jet noise? How are the noise sources distributed in space and time? Answering these questions could lead to innovative strategies for controlling jet noise. The technique could also be further developed to account for the presence of solid boundaries. This would be of great interest to improve the understanding of how solid surfaces may give rise to sound sources and affect the sound generated by nearby turbulence.

---

[*]Research fellow, ISVR, University of Southampton
[†]Lecturer, Department of Engineering, University of Cambridge
[‡]Senior lecturer, School of Engineering Sciences, University of Southampton

American Institute of Aeronautics and Astronautics

The flows of practical interest are usually turbulent and involve a broad range of frequencies. However, the algorithm proposed by Sinayoko *et al.*[6] employed only spatial filtering, which is sufficient only when acoustic radiation is dominated by a single frequency. For a turbulent flow, spatio-temporal filters should be employed. Understanding how to to do this efficiently is crucial for computing the sound sources in a general flow. In this paper, we address this issue by presenting an algorithm for computing the sound sources at multiple frequencies. The sources are then computed for a laminar axisymmetric jet, and the mechanism responsible for most of the noise generation is identified. Finally, the sources are computed for a fully turbulent subsonic jet, obtained from a Direct Numerical Simulation of the Navier-Stokes equations.

I. Non-radiating base flow sources

I.A. Definition

We assume an unbounded, homentropic, perfect gas jet flow of a low Reynolds number ($< 10^4$ based on jet diameter and exit velocity). Although restrictive, these conditions are sufficient to capture the sound generation from large scale structures in subsonic jets.[7] Other effects due to the presence of, for example, solid boundaries,[8] temperature gradients[9] or supersonic speeds[10] will be ignored for simplicity.

The flow satisfies the following equations:[6]

$$\frac{\partial \rho}{\partial t} + \frac{\partial}{\partial x_j}\rho v_j = 0, \tag{1}$$

$$\frac{\partial}{\partial t}\rho v_i + \frac{\partial}{\partial x_j}\rho v_i v_j + \frac{\partial}{\partial x_i}\pi^\gamma = 0, \tag{2}$$

$$\frac{\partial \pi}{\partial t} + \frac{\partial}{\partial x_j}\pi v_j = 0. \tag{3}$$

where ρ denotes the density, $\mathbf{v}$ the velocity field, $\pi = p^{1/\gamma}$ the modified pressure field, where p is the pressure field and γ the specific heat ratio.

Using $\mathbf{q} = \{\rho, \rho\mathbf{v}, \pi\}$ as the set of dependent variables, each flow variable q can be decomposed as

$$q = \bar{q} + q', \tag{4}$$

where $\bar{q}$ denotes the non-radiating part of q and q' the radiating part. The radiating part corresponds to the acoustic part of q in the far field.

The radiating components $\mathbf{q}'$ satisfy an equation of the form[6]

$$\mathbf{L}(\mathbf{q}') = \mathbf{s}, \tag{5}$$

where $\mathbf{L}$ is a linear operator, $\mathbf{s} = \{0, \mathbf{f}, 0\}$ and $\mathbf{f}$ represents the momentum equation source term defined as

$$f_i = -\frac{\partial}{\partial x_j}\left(\bar{\rho}\,\widetilde{v}_i\widetilde{v}_j\,\right)'. \tag{6}$$

In equation (6), $\widetilde{v}_i = \overline{\rho v_i}/\bar{\rho}$ denotes Favre averaged velocity. The non-radiating base flow (NRBF) source $\mathbf{f}$ depends only on the non-radiating flow variables $\bar{\mathbf{q}}$. The full system of equation is given in appendix A. It must be used to propagate the sound generated by the NRBF source $\mathbf{f}$.

I.B. Algorithm for the non-radiating base flow decomposition

The expression of equation (6) for the NRBF sources requires a decomposition of the flow variables into radiating and non-radiating components. An algorithm has been proposed[6] for a single-frequency radiating field. Here we derive a more general algorithm, applicable to radiating flow fields composed of multiple frequencies. It shows how to carry out the NRBF decomposition efficiently for a general flow field.

For a flow variable q, the non-radiating field $\bar{q}$ is computed as follows:

1. Identify the discrete frequencies $\omega_1, \omega_2, \ldots \omega_N$ which dominate the far field by examining the power spectral density of q in the far field.

2. For each radiating frequency ω_r, compute $q_{\omega_r}(\mathbf{x}, t)$, which represents the instantaneous contribution of frequencies $\pm\omega_r$ to $q(\mathbf{x}, t)$ and is defined as

$$q_{\omega_r}(\mathbf{x}, t) = \frac{1}{2\pi} \left[Q(\mathbf{x}, \omega_r)e^{-j\omega t} + Q(\mathbf{x}, -\omega_r)e^{j\omega t} \right], \tag{7}$$

where $Q(\mathbf{x}, \omega)$ is the Fourier transform in time of $q(\mathbf{x}, t)$:

$$Q(\mathbf{x}, \omega) = \int_{-\infty}^{+\infty} q(\mathbf{x}, t)e^{i\omega t}\, dt. \tag{8}$$

Since, $q(\mathbf{x}, t)$ is real, $Q(\mathbf{x}, -\omega_r)$ is the complex conjugate of $Q(\mathbf{x}, \omega_r)$ so equation (7) can be written

$$q_{\omega_r}(\mathbf{x}, t) = \frac{1}{\pi} \left[Q^R(\mathbf{x}, \omega_r) \cos(\omega_r t) + Q^I(\mathbf{x}, \omega_r) \sin(\omega_r t) \right], \tag{9}$$

where the R and I superscripts denote the real and imaginary parts. Equation (9) allows us to compute $q_{\omega_r}(\mathbf{x}, t)$, *for any time t*, from the real and imaginary parts of $Q(\mathbf{x}, \omega_r)$.

3. For a given time t, for each value of ω_r, compute the radiating part $q'_{\omega_r}(\mathbf{x}, t)$ of $q_{\omega_r}(\mathbf{x}, t)$ by using the following procedure:

   - compute the Fourier transform in space of $Q^R(\mathbf{x}, \omega_r)$, denoted $\mathcal{Q}(\mathbf{k}, \omega_r)$,
   - multiply $\mathcal{Q}(\mathbf{k}, \omega_r)$ by a filter window $\mathcal{G}(\mathbf{k}, \omega_r)$ designed to return the radiating components (see section I.C), which gives $\mathcal{Q}'(\mathbf{k}, \omega_r)$,
   - compute the real part of the inverse Fourier transform in space of $\mathcal{Q}'(\mathbf{k}, \omega_r)$, i.e. $Q^{R'}(\mathbf{x}, \omega_r)$,
   - repeat the above steps with $Q^I(\mathbf{x}, \omega_r)$ instead of $Q^R(\mathbf{x}, \omega_r)$ to get $Q^{I'}(\mathbf{x}, \omega_r)$,
   - compute $q'_{\omega_r}(\mathbf{x}, t)$ from equation (9).

4. Compute the radiating part $q'(\mathbf{x}, t)$ as

$$q'(\mathbf{x}, t) = \sum_{r=1}^{N} q'_{\omega_r}(\mathbf{x}, t) \tag{10}$$

5. Compute the non-radiating field $\overline{q}(\mathbf{x}, t)$ as

$$\overline{q}(\mathbf{x}, t) = q(\mathbf{x}, t) - q'(\mathbf{x}, t). \tag{11}$$

In the above algorithm, step 3 greatly reduces the computational cost of the flow decomposition, in terms of both processing time and memory requirements. To obtain $\overline{q}(\mathbf{x}, t)$, we only need to compute the radiating part of $Q(\mathbf{x}, \omega_r)$ for the dominant radiating frequencies ω_r. This is cheaper than computing the full Fourier transform in time and space of $q(\mathbf{x}, t)$ and applying a filter defined over all frequencies and wavenumbers.

I.C. Filter window

For several different families of flows commonly found in practical applications, for every frequency ω, the radiating components lie on a simple surface $S(\omega)$ in the wavenumber domain. In such cases, the ideal filter window for computing the radiating components in the frequency-wavenumber domain is defined as

$$\mathcal{G}(\mathbf{k}, \omega) = 1 \quad \text{if} \quad \mathbf{k} \in S(\omega) \tag{12}$$
$$\mathcal{G}(\mathbf{k}, \omega) = 0 \quad \text{if} \quad \mathbf{k} \notin S(\omega). \tag{13}$$

If the flow is uniform in the far field, then $S(\omega)$ is an ellipse. If the coordinate system (x, y, z) is chosen such that $\mathbf{v} = (0, 0, M_\infty c_\infty)$, then the ellipse is defined[11] as

$$\frac{k_x^2}{b^2} + \frac{k_y^2}{b^2} + \frac{(k_z - k_0)^2}{a^2} = 0, \tag{14}$$

American Institute of Aeronautics and Astronautics

where

$$k_0 = -\frac{M_\infty}{1 - M_\infty^2}\frac{\omega}{c_\infty}, \quad a = \frac{1}{1 - M_\infty^2}\frac{\omega}{c_\infty}, \quad b = \frac{\omega}{c_\infty}\frac{1}{\sqrt{1 - M_\infty^2}}. \tag{15}$$

If the flow is quiescent in the far field, then $S(\omega)$ is a sphere[5, 12] defined as $|\mathbf{k}| = \omega/c_\infty$, where c_∞ is the speed of sound in the far field. In the rest of this section, we will assume that $M_\infty = 0$ for simplicity.

In the physical domain, the filter is obtained by taking the inverse space–time Fourier transform of $\mathcal{G}$:

$$g(\mathbf{x}, t) = \frac{\delta'(t - |\mathbf{x}|/c_\infty)}{4\pi^2 c_\infty |\mathbf{x}|} - \frac{\delta'(t + |\mathbf{x}|/c_\infty)}{4\pi^2 c_\infty |\mathbf{x}|}, \tag{16}$$

where δ' is the derivative of the Dirac delta distribution. For a harmonic signal at frequency ω, the filter is obtained by taking the spatial inverse Fourier transform of $\mathcal{G}$:

$$G(\mathbf{x}, \omega) = \frac{1}{4\pi^2}k^2\mathrm{sinc}(k|\mathbf{x}|), \quad \text{where} \quad k = \omega/c_\infty. \tag{17}$$

Most of the energy of the filter is contained in the main lobe of width $\lambda = 2\pi/k$. The filter becomes broader as ω tends to 0.

A Gaussian filter can be used to approximate the ideal filter in numerical applications:

$$\mathcal{G}(\mathbf{k}, \omega) = \exp\left[-\frac{(|\mathbf{k}| - \omega/c_\infty)^2}{2\sigma^2}\right], \tag{18}$$

where σ can be frequency dependent. For small values of σ, the Gaussian filter behaves like the ideal filter.

The parameter σ must be chosen to allow the separation of radiating and non-radiating components. It requires careful examination of the spatio-temporal Fourier transform of the flow field. The temporal Fourier transform is carried out before the spatial Fourier transform. Let $Q = Q^R + iQ^I$ denote the temporal Fourier transform of the input field q. Let $\mathcal{Q}^R$ and $\mathcal{Q}^I$ denote the spatial Fourier transforms of Q^R and Q^I. It is natural to apply the filter $\mathcal{G}$ to $\mathcal{Q} \equiv \mathcal{Q}^R + i\mathcal{Q}^I$. However, the visual identification of the radiating and non-radiating components appears easier for $|\mathcal{Q}^R|$ and $|\mathcal{Q}^I|$ than for $|\mathcal{Q}^R + i\mathcal{Q}^I|$, as done in step 3 of I.B. We therefore recommend to filter Q^R and Q^I separately.

I.D. Computation of the spatio–temporal Fourier transform

The temporal Fourier transform can be obtained for a range of discrete frequencies by using a discrete Fourier transform. This can be done, for example, by using the Fast Fourier Transform[13] (FFT). However, the FFT computes the Fourier transform of the input signal over all discrete frequencies. If only a few frequencies are dominating the radiating field, a direct Fourier transform algorithm, such as Goertzel's algorithm,[14] can be used. This is especially important for three-dimensional flow fields. The dominant radiating frequencies can be determined beforehand by computing the power spectral density in the far field.

The computation of the spatial Fourier transform varies with the geometry of the flow field. If the data is laid out over a cartesian grid, one can use the FFT in each direction. If the data is laid out over a cylindrical grid, for example for a round jet, then the Fourier transform is computed as follows: the data is first decomposed by means of a Fourier series in the azimuthal direction, for example, by using the FFT. The azimuthal mode of order n is then Fourier transformed in the radial direction by means of a Hankel transform of the first kind of order n, followed by a Fourier transform in the axial direction. For an axisymmetric flow field, one should apply a Hankel transform of order 0 in the radial direction, except for the radial velocity, for which a Hankel transform of order one is necessary.[6]

Finally, the product of the filter window $\mathcal{G}$ with the flow variable $\mathcal{Q}$ in the Fourier domain can introduce some aliasing in the physical domain. To avoid this, the discrete data is zero padded in all directions of space and time. If the input data is of length N in a particular direction, then N zeros are added at the end.

II. NRBF sources in an axisymmetric laminar jet

II.A. Numerical simulation

We consider a nonlinear problem in which an axisymmetric jet is excited by two discrete-frequency axisymmetric disturbances at the jet exit. The frequencies are chosen to trigger some instability waves in the flow.

These instability waves grow downstream and interact non-linearly, generating acoustic waves. The Mach number of the jet is 0.9 and the Reynolds number is 3600. The base mean flow is chosen to match the experimental data of Stromberg *et al.*[15]

Suponitsky *et al.*[16] performed direct numerical simulations of the compressible Navier–Stokes equations for this problem. In their simulations the mean flow was prescribed by imposing time-independent forcing terms. They ran simulations with different combinations of excitation frequencies and amplitudes. The data used here corresponds to the combination with the largest acoustic radiation. The two excitation frequencies are $\omega_1 = 2.2$ and $\omega_2 = 3.4$. Sound radiates mainly at the difference frequency $\Delta\omega = 1.2$. The results presented in this section have been normalised by using the jet diameter D, jet exit speed U_j and the ambient density as the length, velocity and density scales, respectively.

II.B.   Non radiating base flow sources

Flow decomposition

The three frequencies dominating the far field sound are, in decreasing order of importance, 1.2, 1.0 and 2.2. The contribution of other frequencies to the power spectral density (PSD) at point $(z, r) = (40, 20)$, for example, located in the far field in a region of strong acoustic radiation, is at least 20 decibels weaker than the contribution of the peak frequency (1.2). Hence it is sufficient to concentrate on the radiating frequencies $\{1.0, 1.2, 2.2\}$ to compute the radiating sound.

We use a Gaussian filter defined in the frequency–wavenumber domain as

$$\mathcal{W}(\mathbf{k}, \omega) = \exp\left[-\frac{(|\mathbf{k}| - |\omega|/c_\infty)^2}{2\sigma^2} \right].$$

(19)

We want the width of the Gaussian, controlled by σ, to be small to separate the radiating components from the non-radiating components. However, in the physical domain, the filter is a Gaussian of standard deviation $1/\sigma$; as σ tends to zero, the filter width increases in the physical domain which leads to inaccuracies near boundaries. Thus, there is a trade-off between the filter widths in the spectral and physical domains. Here, we have chosen $\sigma = 0.37$ after careful examination of the filtered flow fields in the two domains.

The algorithm of section I.B is applied to the density field ρ. Results are shown in figure 1. The first row (figures 1(a–c)) presents snapshots of $\rho_{1.0}$, $\overline{\rho}_{1.0}$ and $\rho'_{1.0}$, i.e. the NRBF decomposition of the density field at frequency 1.0. Similarly, the second and third rows respectively present similar decompositions at frequencies 1.2 and 2.2. The last row presents the full density field ρ followed by $\overline{\rho}$ and ρ'.

The decomposition is successful: the flow fields in the second column of figure 1, which contain the non-radiating signals, are silent (no sound is propagating to the far field). On the contrary, in the third column, which contains only radiating components, the flow fields are acoustic in nature and contain no hydrodynamic fluctuations.

The decomposition is superior to the one presented by Sinayoko *et al.*,[6] in which the flow field was filtered in the wavenumber domain only by focusing on the dominant radiating frequency $\omega = 1.2$. The proposed algorithm offers an efficient way of decomposing a general flow field containing a broad range of frequencies into its non-radiating and radiating components.

NRBF sources

We present the NRBF sources at frequency 1.2. Similar results have been obtained for the other two radiating frequencies, 1.0 and 2.2. From equation (6), the computation of the axial and radial NRBF sources requires a second filtering step that is applied to $-\partial\left(\overline{\rho}\,\widetilde{\mathbf{v}}\widetilde{v}_j\right)/\partial x_j$. This filtering operation has been carried out by means of a Gaussian filter of standard deviation σ, defined as

$$\sigma(\omega_r) = \frac{1}{7.5}\frac{\omega_r}{c_\infty}.$$

(20)

The above equations can be expressed as $\sigma \approx 1/1.2\lambda$, where $\lambda = 2\pi c_\infty/\omega_r$ denotes the acoustic wavelength. Therefore, in the physical domain, the standard deviation of the filter $(1/\sigma)$ is about one acoustic wavelength.

The filter width defined above for the source computation is different from the constant width $\sigma = 0.37$ used for the flow decomposition of figure 1. The latter value is respectively 3, 2.5 and 1.4 times larger than the width of the filter used for the source computation at frequencies 1.0, 1.2 and 2.2. Thus the filter used
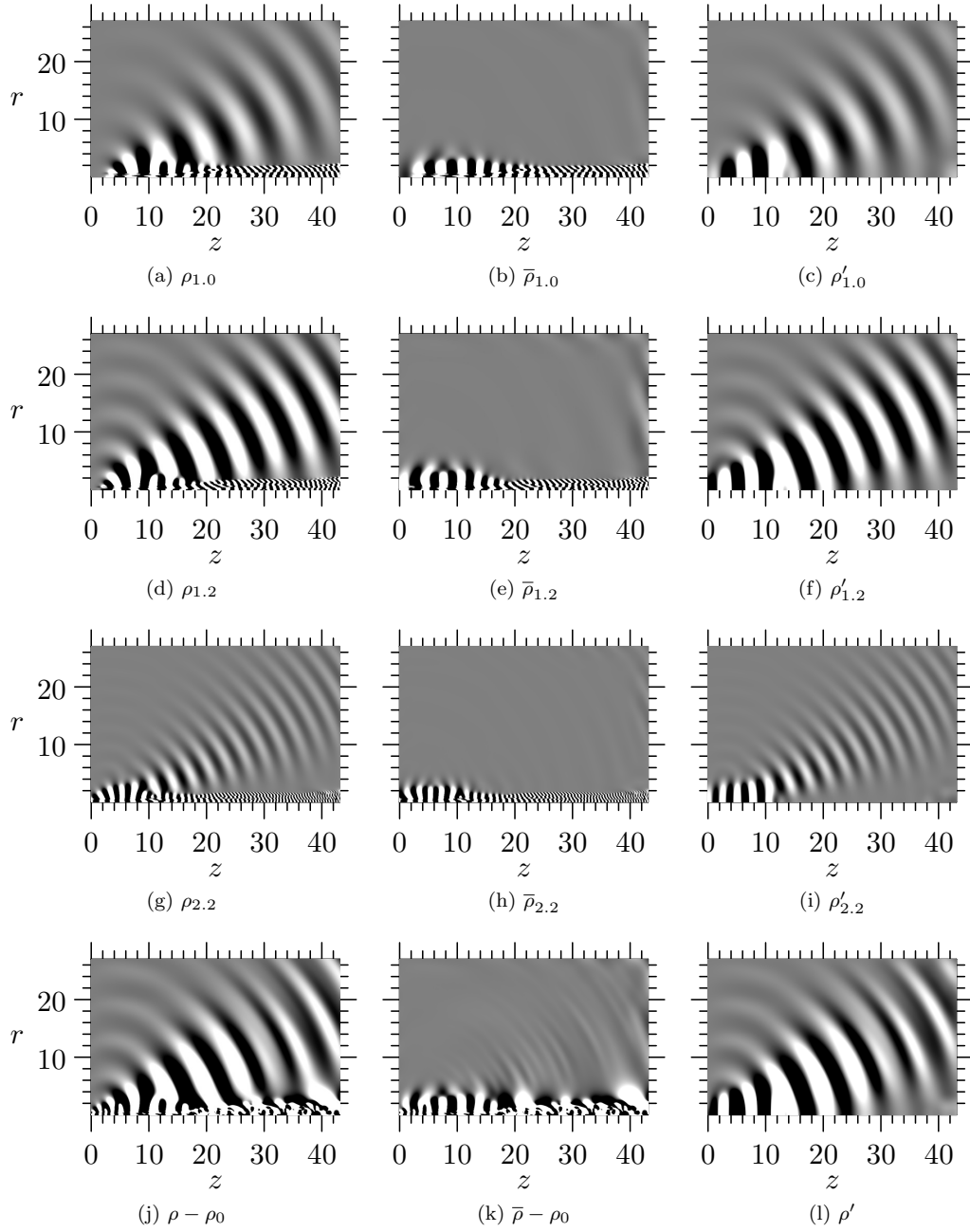
American Institute of Aeronautics and Astronautics

Figure 1: Decomposition of the density field ρ into non-radiating components $\overline{\rho}$ and radiating components ρ'. The field ρ_{ω_r}, where $\omega_r \in \{1.0, 1.2, 2.2\}$, denotes snapshots of the density field at the radiating frequencies. The color scales are from -2×10^{-5} to 2×10^{-5}.

for the flow decomposition is wider in the spectral domain. Using a wider filter is possible because of the clear separation between the radiating and non-radiating components. However, there is no clear separation between the radiating and non-radiating components in the Fourier transform of the term $-\partial \left(\overline{\rho} \, \widetilde{\mathbf{v}} \widetilde{v}_j \right) / \partial x_j$, and the value of σ therefore controls the energy of the NRBF sources. There is no simple way of guessing the right value of σ for the source computation. As will be shown later, equation (20), which has been defined empirically, leads to satisfactory results for the present flow. It remains to be investigated if this equation is applicable to more general flows. Nevertheless, we have observed that the structure of the NRBF sources remains the same for a broad range of values of σ. The physical behaviour of the NRBF sources is therefore relatively insensitive to the value of σ.

Since the flow is axisymmetric, any vector variable $\mathbf{q}$ is expressed in terms of an axial component q_z and

American Institute of Aeronautics and Astronautics

a radial component q_r. The divergence of $\mathbf{q}$ is given by

$$\frac{\partial q_j}{\partial x_j} = \frac{1}{r}\frac{\partial(rq_r)}{\partial r} + \frac{\partial q_z}{\partial z}. \tag{21}$$

Note also that the three-dimensional Fourier transform of an axisymmetric scalar variable $q(r,z)$ is given by its Hankel transform of order 0 in the radial direction, combined with its Fourier transform in the axial direction. To compute the three dimensional Fourier transform of a vector $\mathbf{q}$ expressed as (q_r, q_z), one can use the above technique for the axial component q_z. For the radial component q_r, one should use a Hankel transform of order 1 instead of a Hankel transform of order 0.[6]

Snapshots of $(f_z)_{1.2}$ and $(f_r)_{1.2}$, the momentum-equations NRBF sources at frequency 1.2, are presented in figures 2(a) and 2(b) respectively. The axial NRBF source f_z takes the form of a wave-packet centered around the jet axis. The envelope of the wavepacket reaches a maximum at $z = 5$, which corresponds to the end of the potential core, and becomes negligible for $z \geq 20$. The radial NRBF source f_r is concentrated outside the jet but close to the jet axis, around $r = 2$. It is negligible for $z \geq 5$. Despite the different flow
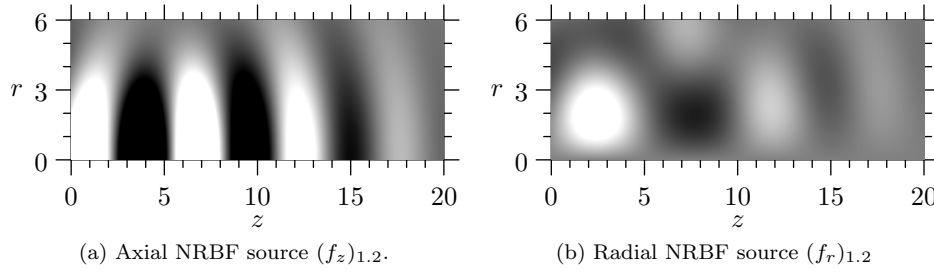

(a) Axial NRBF source $(f_z)_{1.2}$.　　　　　(b) Radial NRBF source $(f_r)_{1.2}$

Figure 2: Snapshots of NRBF sources $(f_z)_{1.2}$ and $(f_r)_{1.2}$ at frequency 1.2. Color scales are from -2×10^{-6} to 2×10^{-6}.

decomposition algorithm, these results are consistent with the ones presented by Sinayoko et $al.$[6]

Validation

To validate the NRBF sources, we propagate the sound to the far field by solving the Euler Equations linearised about the time averaged base flow. These equations do not utilise the linear operator $\mathbf{L}$ on the left hand side of equation (5), but they should be a good approximation for it.[6]

The propagated sound is compared to the radiating part of the DNS solution. The results are presented in figure 3. The DNS solution 3(a) is in good agreement with the sound radiating from the NRBF sources 3(b). A quantitative comparison along $r = 20$ [figure 3(c)] confirms this. These results suggest that the NRBF sources capture the main sound generation mechanism.

(a) $\rho'_{1.2}$ from DNS　　　　(b) $\rho - \rho_0$ from LEE　　　　(c) profiles of $\rho - \rho_0$ and $\rho'_{1.2}$ for $r = 20$
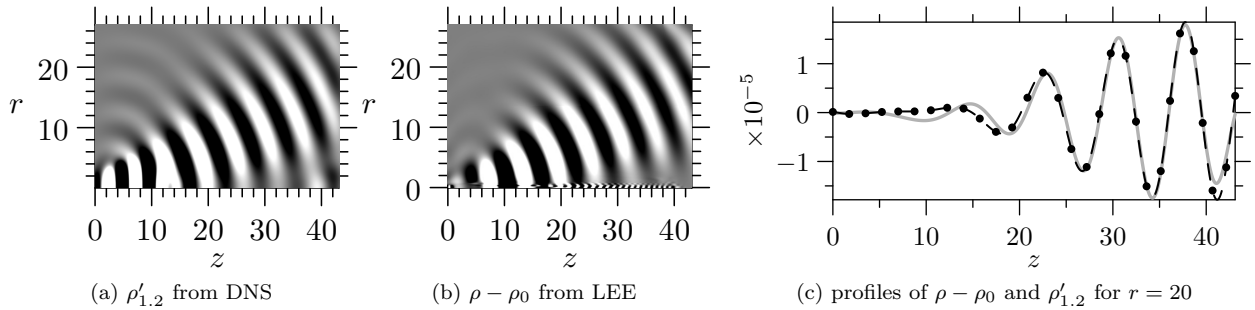
Figure 3: Comparison of (a) the radiating density field $\rho'_{1.2}$ with (b) the density field $\rho - \rho_0$ obtained by driving the LEE with the NRBF sources $(f_z)_{1.2}$ and $(f_r)_{1.2}$. Color scales are from -2×10^{-5} to 2×10^{-5}. Figure (c) gives profiles along $r = 20$: the grey line represents the DNS solution $(\rho_{1.2})$ and the dashed black line with black circles the LEE solution $(\rho - \rho_0)$.

II.C.   Source identification

Decomposition of the NRBF sources

The expression of equation (6) can be further decomposed to identify the radiating core of the NRBF sources. In an axisymmetric flow, the NRBF sources in the momentum equation can be written as

$$f_z = f_{zz} + f_{zr}, \qquad\qquad f_r = f_{rz} + f_{rr}, \qquad\qquad (22)$$

where

$$f_{zz} = -\frac{\partial}{\partial z}\left(\overline{\rho}\widetilde{v}_z\widetilde{v}_z\right)', \qquad\qquad f_{zr} = -\frac{1}{r}\frac{\partial}{\partial r}\left(r\overline{\rho}\widetilde{v}_z\widetilde{v}_r\right)' \qquad\qquad (23)$$

$$f_{rz} = -\frac{\partial}{\partial z}\left(\overline{\rho}\widetilde{v}_z\widetilde{v}_r\right)', \qquad\qquad f_{rr} = -\frac{1}{r}\frac{\partial}{\partial r}\left(r\overline{\rho}\widetilde{v}_r\widetilde{v}_r\right)'. \qquad\qquad (24)$$

The sound fields from these sources are obtained by driving the LEE with them (see figure 4). It is clear that the cross terms f_{zr} and f_{rz} generate negligible sound compared to the terms f_{zz} and f_{rr}. The axial term f_{zz} is responsible for most of the sound radiation. However, the radial term f_{rr} generates significant sound radiation at large angles to the jet axis. These results are consistent with the findings of Suponitsky et al.[17]

(a) $\mathbf{s} = \{0, (f_{zz})_{1.2}, 0, 0\}$ (b) $\mathbf{s} = \{0, (f_{zr})_{1.2}, 0, 0\}$ (c) $\mathbf{s} = \{0, 0, (f_{rz})_{1.2}, 0\}$ (d) $\mathbf{s} = \{0, 0, (f_{rr})_{1.2}, 0\}$
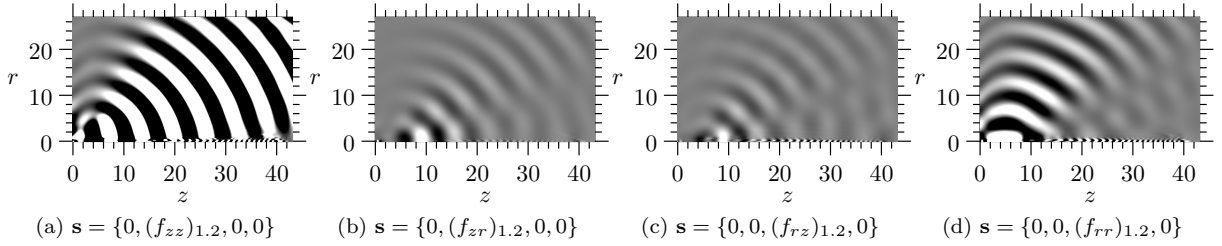
Figure 4: Snapshots of the modified pressure field radiating from the source terms that compose the NRBF sources $(f_z)_{1.2}$ and $(f_r)_{1.2}$, compared to the DNS solution $\rho_{1.2}$. Color scales are from -2×10^{-6} to 2×10^{-6}.

Shear noise

The term f_{zz} can be further decomposed by splitting the non-radiating velocity $\widetilde{v}_z$ into a mean part $\widetilde{v}_{z0}$ and an hydrodynamic parts $\widetilde{v}_z{}''$:

$$\widetilde{v}_z = \widetilde{v}_{z0} + \widetilde{v}_z{}''. \qquad\qquad (25)$$

Note that $\widetilde{v}_{z0}$ is the time-averaged part of $\widetilde{v}_z$ and is therefore different from v_{z0}. In the main sound generating region ($z \leq 15, r \leq 0.5$), we can also assume that $\widetilde{v}_z{}'' \ll \widetilde{v}_{z0}$. If we neglect the effect of density fluctuations, by writing $\overline{\rho} \approx \rho_\infty$, then

$$f_{zz} \approx -\rho_\infty\frac{\partial}{\partial z}\left(\widetilde{v}_{z0}\widetilde{v}_{z0} + 2\widetilde{v}_{z0}\widetilde{v}_z{}'' + \widetilde{v}_z{}''\widetilde{v}_z{}''\right)'. \qquad\qquad (26)$$

The first term in the brackets is steady so its radiating part is zero. The third term is quadratic in the hydrodynamic part of $\widetilde{v}_z$: it can be neglected compared to the second term. Therefore, f_{zz} can be approximated by

$$f_{zz} \approx -2\frac{\partial}{\partial z}\left(\rho_\infty\widetilde{v}_{z0}\widetilde{v}_z{}''\right)'. \qquad\qquad (27)$$

The above expression corresponds to radiating part of the "shear noise" term, which has been identified as the dominant source terms in several studies.[18, 19]

The sound radiating from the "shear noise" term of equation (27) is shown in figure 5. Agreement is very good: the dominant source term in this flow is the shear-noise term.

American Institute of Aeronautics and Astronautics

(a) $\rho'_{1.2}$ from DNS

(b) $\rho - \rho_0$ from LEE

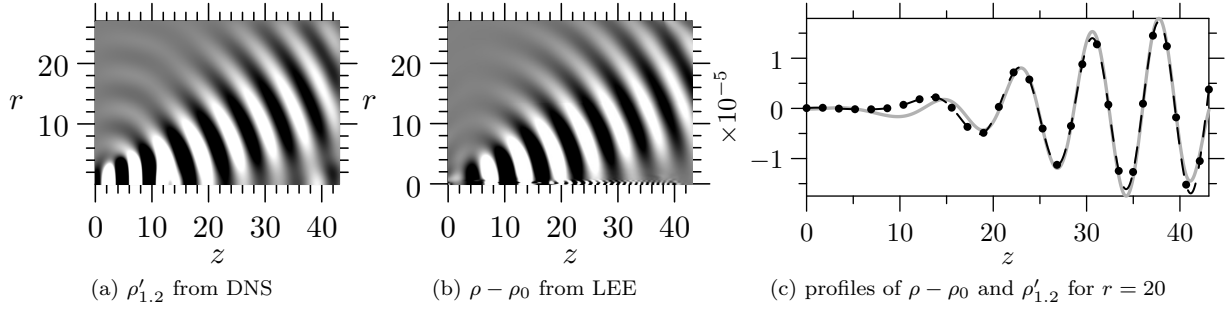(c) profiles of $\rho - \rho_0$ and $\rho'_{1.2}$ for $r = 20$

Figure 5: Comparison of (a) the radiating density field $\rho'_{1.2}$ with (b) the density field $\rho - \rho_0$ obtained by driving the LEE with the shear noise term $(f_{zz})_{1.2}$ of equation (27). Color scales are from -2×10^{-5} to 2×10^{-5}. Figure (c) gives profiles along $r = 20$: the grey line represents the DNS solution ($\rho_{1.2}$) and the dashed black line with black circles the LEE solution ($\rho - \rho_0$).

III.   NRBF sources in a 3D jet

The simulation data is one of several recently performed Direct Numerical Simulations of fully turbulent jets performed by Sandberg et $al.$[20] The simulation includes the nozzle, allowing for a realistic turbulent inflow condition. The jet exits from a round pipe into a co-flow of Mach number $M_\infty = 0.2$. The jet Mach number is $M = 0.84$, and the Reynolds number, based on nozzle diameter, is $Re_D = 7670$. The objective is to demonstrate the feasibility of computing the NRBF sources for a fully turbulent flow field.

III.A.   Modal decomposition and frequency analysis

The power spectral density (PSD) of the density field ρ is studied to uncover the dominant radiating frequencies. Figure 6 presents the PSD at $(z, r, \theta) = (10R, 6R, 0)$ (grey solid line). This point is located within the acoustic region of the near field, as shown in figure 7(a). The peak Strouhal number is $St_D = 0.5$, followed by 0.3 and 0.8. For $St_D \geq 2$, the PSD is at least 10 dB smaller than at the peak frequency. The PSD is also plotted in figure 6 for the cosine part of azimuthal modes 0, 1, 2 and 3. Clearly, the noise radiation is dominated by the axisymmetric mode in that region of the flow field.
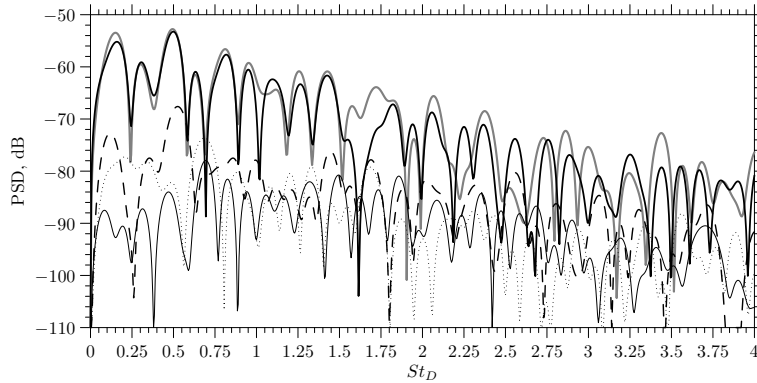

Figure 6: The grey solid line is the power spectral density (PSD) in the near-field for $(z, r, \theta) = (10R, 6R, 0)$. The corresponding PSD at $(z, r) = (10R, 6R)$ is given for modes 0 (thick black line), 1 (dashed line), 2 (dotted line) and 3 (thin black line). In each case the cosine part of the mode has been used. The PSD has been computed as $10 \log(|Q(St)|^2/T)$, where T is the duration of the signal.

In this paper, we focus our efforts on the modes and frequencies that dominate the radiating field. From figure 6, it is reasonable to approximate the radiating part of the density field as the radiating part of the azimuthal modes 0 and 1 for $St_D \leq 4$:

$$\rho(r, \theta, z, t)' \approx \widehat{\rho}_0(r, z, t)' + \widehat{\rho}_c(r, z, t)' \cos(\theta) + \widehat{\rho}_s(r, z, t)' \sin(\theta), \tag{28}$$

American Institute of Aeronautics and Astronautics

where $\widehat{\rho}_0$ is the axisymmetric part of ρ, and $\widehat{\rho}_c$ and $\widehat{\rho}_s$ denote respectively the cosine and sine part of the first azimuthal mode. A snapshot of $(\widehat{\rho}_0 + \widehat{\rho}_c)_{|St_D|\leq 4}$, over the entire computational domain, is plotted in figure 7(b). The similarity of the radiating field in 7(b) compared to 7(a) shows that equation (28) is a good approximation. Computing the radiating part of ρ reduces to filtering $\widehat{\rho}_0$, $\widehat{\rho}_c$ and $\widehat{\rho}_s$, for Strouhal numbers up to four. Note that the sine and cosine parts are two-dimensional, whereas ρ is three dimensional. Thus, equation (28) reduces a three dimensional flow decomposition problem to a series of two-dimensional decomposition problems. Each two-dimensional field can be filtered by applying the methods developed for the axisymmetric jet of section II. Finally, one could add higher-order modes to the right hand side of equation (28) to improve the accuracy of the flow decomposition.
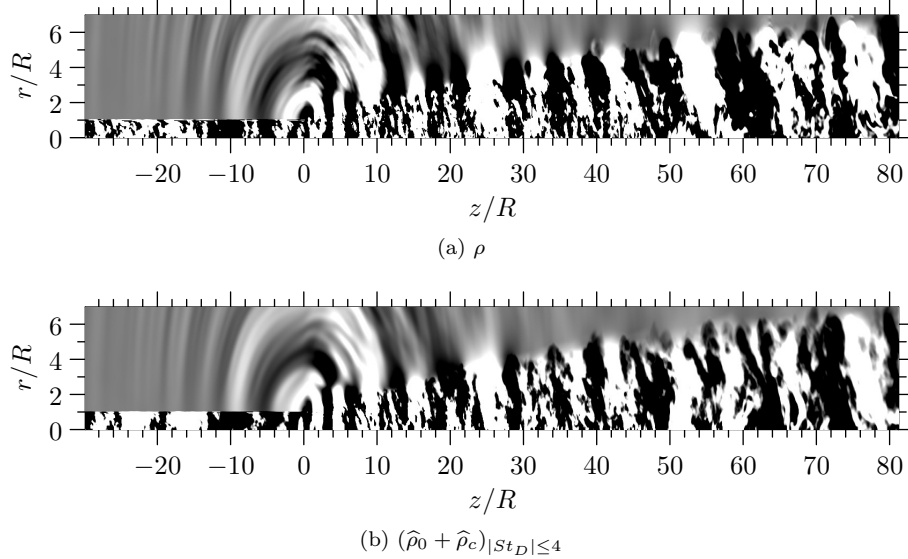

(a) ρ

(b) $(\widehat{\rho}_0 + \widehat{\rho}_c)_{|St_D|\leq 4}$

Figure 7: Snapshots, for $\theta = 0$, of (a) ρ and (b) $(\widehat{\rho}_0 + \widehat{\rho}_c)_{|St_D|\leq 4}$, using the notations of equation (28). The color scale is between -5×10^{-4} and 5×10^{-4}. The similarity of the radiating field in (b) relative to (a) shows that most of the radiating field is contained within azimuthal modes 0 and 1 and $|St_D| \leq 4$, which validates equation (28).

III.B. Flow decomposition

The temporal Fourier transform is computed using Goertzel's algorithm,[14] with 320 time frames and time step $\Delta t = 0.625$. The data is zero padded with 320 extra time frames so the result can be filtered without aliasing effects. Thus, the computed Strouhal numbers are separated by $\Delta St_D = 0.05$. The spatial Fourier transform of mode n is carried out using the FFT in the axial direction, and the Quasi Discrete Hankel Transform[21] of the first kind of order n in the radial direction. The top row of figure 8 presents, on the left hand side, the real part of the temporal Fourier transform of ρ at $St_D = 1.1$ and, on the right hand side, the spatio-temporal Fourier transform of ρ at $St_D = 1.1$. The nozzle is not included in the computation. It is clear that the sound is originating from a region very close to the jet exit. The computation of the non-radiating sources is difficult near boundaries[6] so it is preferable to include the nozzle in the computation of the sound sources.

The result of including the nozzle in the computation of the Fourier transform is shown in the bottom row of figure 8 for $St_D = 1.1$. The presence of the nozzle affects the distribution of the radiating components in the wavenumber domain. If the nozzle is included, the radiating components are spread out along a vertical line ($k_z \approx 1.8$ in this case) mostly included within the radiation ellipse. In contrast, if the nozzle is not included, the radiating components follow the radiation ellipse of equation (14). Because of this, we use the following filter to remove the radiating components:

$$\mathcal{W}(k,\theta) = \frac{1}{2}\left[1 - \tanh\left(\frac{k - k_e(\theta)}{\sigma}\right)\right], \quad k_e(\theta) = \frac{ab}{\sqrt{b^2\cos^2\theta + a^2\sin^2\theta}} \tag{29}$$

where k and θ are polar coordinates taken using the center of the radiation ellipse as the origin, i.e. $(-k_0, 0)$,
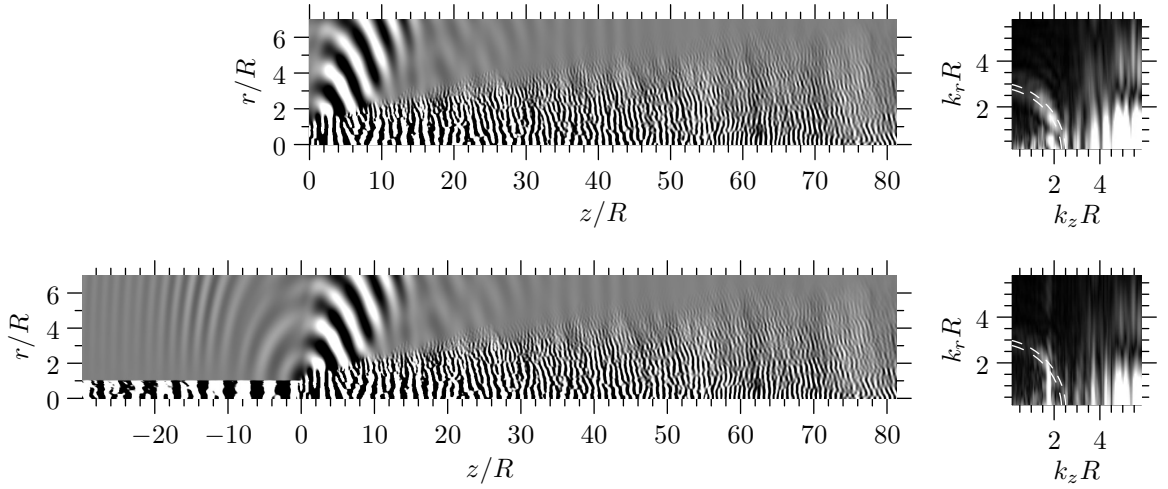
Figure 8: The left column shows the real part of the temporal Fourier transform of $\widehat{\rho}_0$ for $St_D = 1.1$. The right column presents the corresponding spatial Fourier transform. The dashed white line indicate the radiation region and are separated by $\Delta k = \sqrt{\Delta k_r + \Delta k_z} \approx 0.22$. The computation is carried out without the nozzle in the first row and with the nozzle in the second row. When the nozzle is present, the acoustic components are mostly distributed on a vertical line inside the radiation ellipse. Colour scales are between -2×10^{-5} and 2×10^{-5} in the left column and between 0 and 0.018 in the right column.

and where k_0, a and b have been defined in equation (15). The term $k_e(\theta)$ represents the radius of the ellipse in the direction θ. The parameter σ controls the steepness of the cut-off. It has been defined as

$$\sigma = \max\left(\frac{1}{7.5}\frac{\omega}{c_\infty}, 1.2\Delta k\right), \tag{30}$$

so that σ is at least equal to $1.2\Delta k$, where $\Delta k = 0.22$. The filter is designed to remove all the components that are inside of the radiation ellipse.

The result of decomposing the density field for modes 0 and 1 is shown in figure 9. The top three rows present the filtering of ρ for mode 0 and Strouhal numbers of 0.5, 0.8 and 1.45. The first column gives ρ, while the second and third columns present ρ' and $\bar{\rho}$, which have been obtained by applying the algorithm of section I.B with the filter window of equation (29). The subfigures (c), (f) and (i) of figures 9 demonstrate that the computed value of $\bar{\rho}$ for mode 0 is non-radiating for $z \geq 0$. In the nozzle region, $z < 0$, some ringing effects can be observed. They should have little effect on the computation of the sound sources since the sound sources are distributed *a priori* within the jet itself, for $z \geq 0$. The bottom two rows of figure 9 present the result of filtering the modes 0 and 1 for a broad range of frequencies, ranging from $St_D = 0.5$ to $St_D = 4.0$. For each mode, the non-radiating field is computed successfully. The filter has not been applied for $St_D < 0.5$ due to a poor resolution of the Fourier transform in the radial direction. For these frequencies, the acoustic wavelength λ is greater than $5.5R$ and the domain is too narrow ($r_{max} = 7$) to compute the two-dimensional spatial Fourier transform accurately. From figure 6, there are significant radiating components left within $\bar{\rho}$. However, the adverse effect on the source computation is expected to be minor. Sinayoko *et al.*[22] have indeed found that, for the axisymmetric jet of section II, assuming $\bar{q} = q$ does allow to capture the dominant sources of sound.

III.C.   Sound sources

The axial NRBF source term f_{zz}, defined as

$$f_{zz} = -\frac{\partial}{\partial z}\left(\bar{\rho}\widetilde{v}_z\widetilde{v}_z\right)', \tag{31}$$

is computed for mode 0 and $St_D = 0.5$, 1.1, 1.45 and 2.55, by using the filter window of equation (29). The results are presented in figure 10. For each Strouhal number, from left to right, the real part F_{zz}^R,
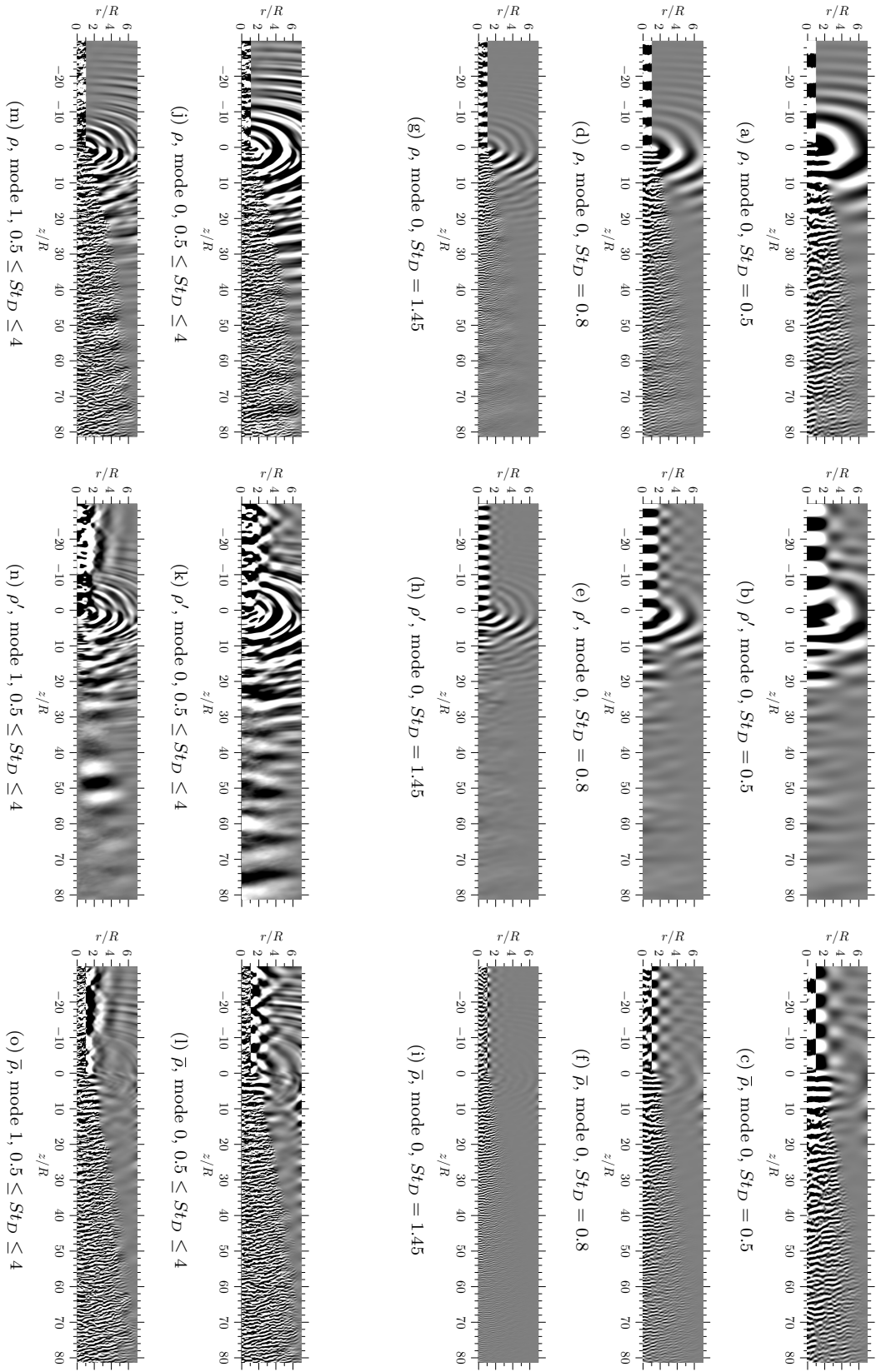
(a) ρ, mode 0, $St_D = 0.5$

(b) ρ', mode 0, $St_D = 0.5$

(c) $\overline{\rho}$, mode 0, $St_D = 0.5$

(d) ρ, mode 0, $St_D = 0.8$

(e) ρ', mode 0, $St_D = 0.8$

(f) $\overline{\rho}$, mode 0, $St_D = 0.8$

(g) ρ, mode 0, $St_D = 1.45$

(h) ρ', mode 0, $St_D = 1.45$

(i) $\overline{\rho}$, mode 0, $St_D = 1.45$

(j) ρ, mode 0, $0.5 \leq St_D \leq 4$

(k) ρ', mode 0, $0.5 \leq St_D \leq 4$

(l) $\overline{\rho}$, mode 0, $0.5 \leq St_D \leq 4$

(m) ρ, mode 1, $0.5 \leq St_D \leq 4$

(n) ρ', mode 1, $0.5 \leq St_D \leq 4$

(o) $\overline{\rho}$, mode 1, $0.5 \leq St_D \leq 4$

Figure 9: Non-radiating decomposition of the density field for azimuthal modes $n = 0$ and 1, i.e. of $\widehat{\rho_0}$ and $\widehat{\rho_c}$ using the notations of equation (28). The top three rows are for $n = 0$ and $St_D = 0.5$, 0.8 and 1.45 respectively. The last two rows are for $n = 0$ and 1 respectively, with $0.5 \leq St_D \leq 4.0$. Color scales are between -5×10^{-5} and 5×10^{-5}.

imaginary part F_{zz}^I and absolute value $|F_{zz}|$ of the temporal Fourier transform of f_{zz} is given. Note that, from equation (9), at any given time, the contribution of frequency ω to f_{zz} is a linear combination of F_{zz}^R and F_{zz}^I, with coefficients $2\cos(\omega t)$ and $-2\sin(\omega t)$. This allows to picture the evolution of each source term over time: the source fluctuates between F_{zz}^R and F_{zz}^I at (normalised) frequency $\omega = \pi St_D$. The absolute value is associated with the distribution of energy within the source.

The structure of the sound source varies with frequency. At low frequency, e.g. $St_D = 0.5$, the source behaves like a wavepacket: there is a structure moving and being amplified from $z = 5R$ to $z = 10R$ (10 a) (the very energetic structure centered on $z = 2R$ in the middle figure behaves like a monopole). The wavepacket reaches its peak near the end of the potential core ($z \approx 10R$) and is located within the jet. This source is very similar to the one observed for the laminar jet of section II. At high frequency, e.g. $St_D = 1.45$, the source also takes the form of a wavepacket but it is centered on the shear layer at $r = R$, and its peak is closer to the jet exit (around $z = 4R$) (10(c)). Structures which do not take the form of wavepackets can be observed for very high frequency: for example, the source at $St_D = 2.55$ has the signature of a vortex pairing, located within the shear layer for $0 \leq z \leq 5$.
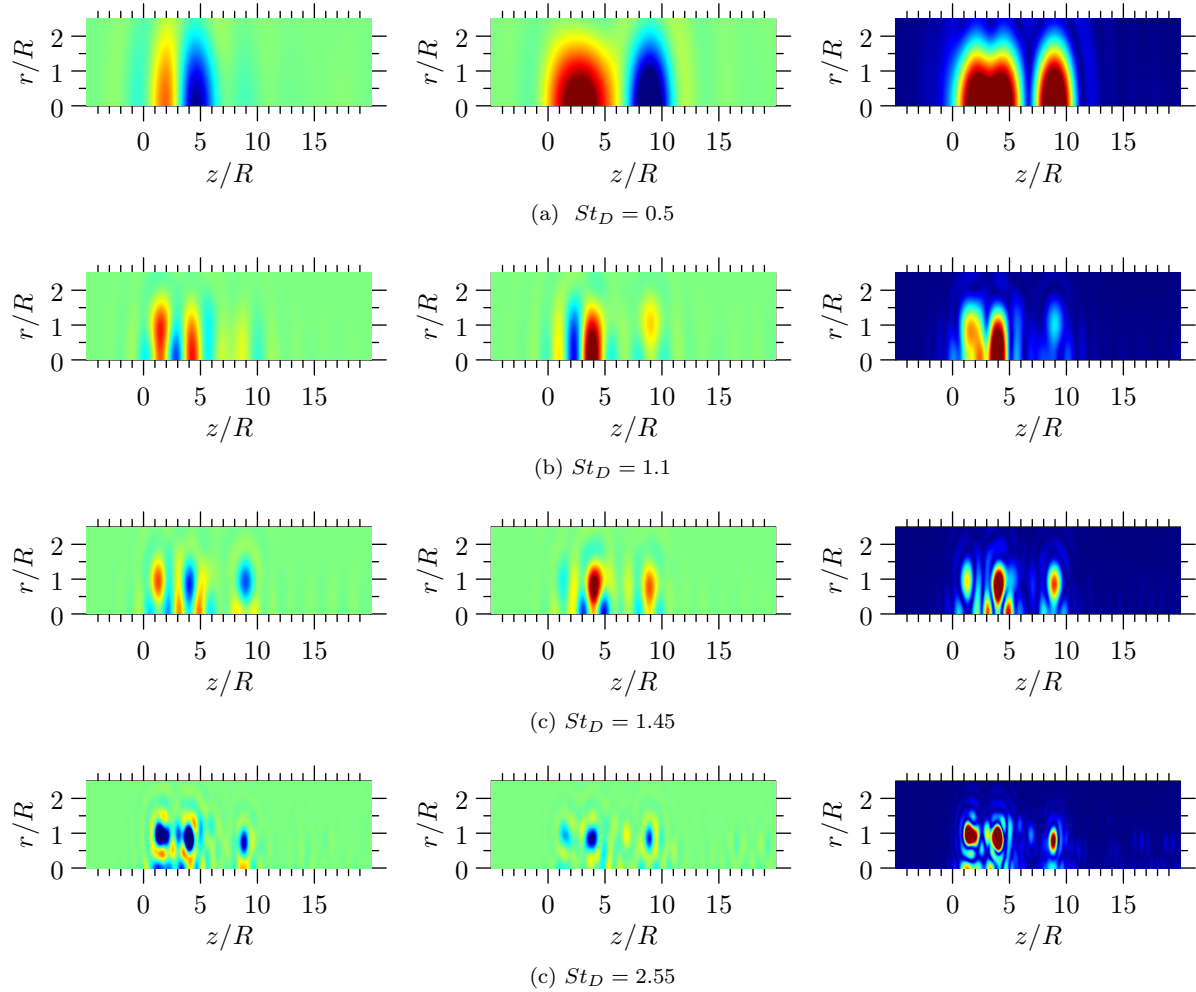

(a) $St_D = 0.5$

(b) $St_D = 1.1$

(c) $St_D = 1.45$

(c) $St_D = 2.55$

Figure 10: NRBF sources f_{zz} for $St_D = 0.5$, 1.1, 1.45 and 2.55. The columns represent, from left to right, the real, imaginary and absolute values of the temporal Fourier transform of f_{zz} for the specified Strouhal number. From top to bottom, the maximum color scale is 0.13, 0.56, 0.76 and 1.0.

The sources can be validated by driving the LEE equations. Unfortunately, if the nozzle is included, instability waves are excited. If the nozzle is not included, the solution develops slightly differently due to the presence of the boundary close to the sound sources. This undesirable effect is weaker at high frequencies. Figure 11 presents a comparison of the radiating density field $\widehat{\rho}_0$ from the DNS, for $St_D = 1.1$, with that obtained by driving the LEE with the source f_{zz} of figure 10(b). The results have been normalised for comparison because the amplitudes do not match well. However, there is good qualitative agreement

between the two fields. This suggest that the computed NRBF source has successfully captured the noise generation mechanism.
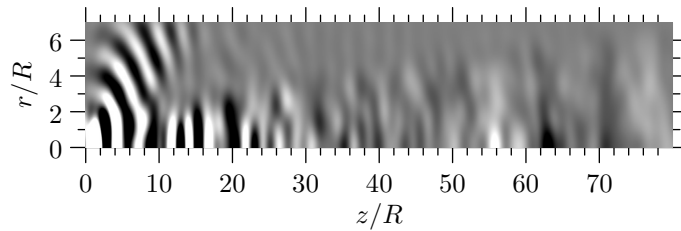
(a) Density ρ' for mode 0 and $St_D = 1.1$, DNS.
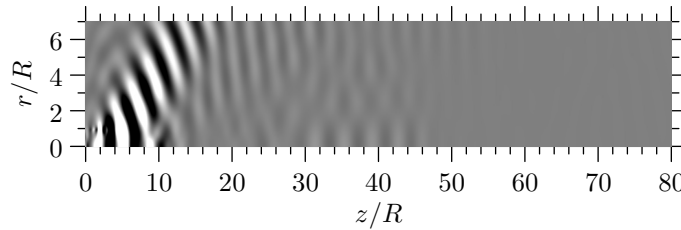
(b) Normalised density $7 \times 10^{-4} \rho'$ for mode 0 and $St_D = 1.1$, LEE.

Figure 11: Comparison of (a) the radiating part of the density field ρ' for mode 0 and $St_D = 1.1$, from the DNS, with (b) the density field obtained by driving the LEE with the NRBF source of figure 10.

Conclusions

The non-radiating base flow (NRBF) sources have been computed for a laminar and a fully turbulent jet. For the laminar jet, the sources have been computed and validated successfully for a Mach 0.9 axisymmetric jet, at three different frequencies. The NRBF sources have two interesting properties: their order of magnitude is similar to that of the sound field, and they are maximum near the end of the potential core. Moreover, the NRBF sources appear to generate little to no hydrodynamic waves when used as source terms on the right hand side of the linearised Euler equations. These findings suggest that the NRBF sources are close to the true sources of sound. In the laminar jet presented in this paper, the dominant noise mechanism is the "shear-noise" term. It involves a product of the mean flow with the hydrodynamic fluctuations, along the jet axis. The source takes the form of a wavepacket whose envelope is non-uniform.

For the fully turbulent jet, the NRBF sources have been computed for the axisymmetric mode of a Mach 0.84 and Reynolds number 7670 jet. For low Strouhal numbers, as in the laminar jet case, the sound sources take the form of wavepackets centered about the jet axis, near the end of the potential core. For higher Strouhal numbers, the sources resemble wavepackets centered on the jet shear layer. The NRBF sources also indicate the presence of two other mechanisms: a monopole located just outside of the jet nozzle and vortex pairings in the shear layer. These results demonstrate the usefulness of the non-radiating base flow decomposition for understanding the generation of aerodynamic noise.

Acknowledgements

A. Governing equations

Using the non-radiating base flow decomposition, the governing equations can be written as:

$$\frac{\partial \rho'}{\partial t} + \frac{\partial}{\partial x_j} \left(\rho v_j \right)' = 0, \tag{32}$$

$$\frac{\partial}{\partial t} \left(\rho v_i \right)' + \frac{\partial}{\partial x_j} \left[\widetilde{v_j}(\rho v_i)' + \widetilde{v_i}(\rho v_j)' - \widetilde{v_i}\widetilde{v_j}\rho' \right]' + \gamma \frac{\partial}{\partial x_i} \left[\overline{\pi}^{\gamma-1}\pi' \right]' = f_i, \tag{33}$$

$$\frac{\partial \pi'}{\partial t} + \frac{\partial}{\partial x_j} \left[\frac{\overline{\pi}}{\overline{\rho}} \left[\left(\rho v_j \right)' - \widetilde{v_j}\rho' \right] + \widetilde{v_j}\pi' \right]' = 0, \tag{34}$$

References

[1] Lighthill, M. J., "On sound generated aerodynamically. I. General theory," *Proceedings of the Royal Society of London*, Vol. 211, No. 1107, 1952, pp. 564–587.

[2] Lilley, G. M., "On the noise from jets," *AGARD Conference Proceedings No.131 on Noise Mechanisms*, Brussels, Belgium, 1974, pp. 13 − 1.

[3] Goldstein, M. E., "A generalized acoustic analogy," *Journal of Fluid Mechanics*, Vol. 488, 2003, pp. 315 − 333.

[4] Bogey, C., Bailly, C., and Juvé, D., "Computation of flow noise using source terms in linearized Euler's equations," *AIAA Journal*, Vol. 40, No. 2, 2002, pp. 235–243.

[5] Goldstein, M. E., "On identifying the true sources of aerodynamic sound," *Journal of Fluid Mechanics*, Vol. 526, 2005, pp. 337 − 347.

[6] Sinayoko, S., Agarwal, A., and Hu, Z., "Flow decomposition and aerodynamic noise generation," *Journal of Fluid Mechanics*, Vol. 668, 2011, pp. 335–350.

[7] Bogey, C., Bailly, C., and Juvé, D., "Noise investigation of a high subsonic, moderate Reynolds number jet using a compressible large eddy simulation," *Theoretical and Computational Fluid Dynamics*, Vol. 16, No. 4, 2003, pp. 273–297.

[8] Ffowcs Williams, J. E. and Hawkings, D. L., "Sound generation by turbulence and surfaces in arbitrary motion," *Philosophical Transactions for the Royal Society of London. Series A, Mathematical and Physical Sciences*, Vol. 264, No. 1151, 1969, pp. 321–342.

[9] Lilley, G. M., "The generation and radiation of supersonic jet noise. Vol. IV - theory of turbulence generated jet noise, noise radiation from upstream sources, and combustion noise. Part II: Generation of sound in a mixing region," *US Air Force Aero Propulsion Lab., AFAPL-TR-72-53, July*, 1972.

[10] Tam, C. K. W., "Supersonic jet noise," *Annual Review of Fluid Mechanics*, Vol. 27, 1995, pp. 17 − 43.

[11] Zhou, L., "Sound directivity generated by spatially developing mixing layer," Private communication.

[12] Crighton, D. G., "Basic principles of aerodynamic noise generation," *Progress in Aerospace Sciences*, Vol. 16, 1975, pp. 31–96.

[13] Shin, K. and Hammond, J. K., *Fundamentals of signal processing for sound and vibration engineers*, Wiley, 2008.

[14] Goertzel, G., "An algorithm for the evaluation of finite trigonometric series," *The American Mathematical Monthly*, Vol. 65, No. 1, 1958, pp. 34–35.

[15] Stromberg, J. L., McLaughlin, D. K., and Troutt, T. R., "Flow field and acoustic properties of a Mach number 0.9 jet at a low Reynolds number," *Journal of Sound and Vibration*, Vol. 72, No. 2, 1980, pp. 159–176.

[16] Suponitsky, V. and Sandham, N. D., "Nonlinear mechanisms of sound radiation in a subsonic flow," *AIAA paper 2009-3317*, 2009.

[17] Suponitsky, V., Sandham, N. D., and Morfey, C. L., "Linear and nonlinear mechanisms of sound radiation by instability waves in subsonic jets," *Journal of Fluid Mechanics*, Vol. 658, 2010, pp. 509–538.

[18] Panda, J., Seasholtz, R. G., and Elam, K. A., "Investigation of noise sources in high-speed jets via correlation measurements," *Journal of Fluid Mechanics*, Vol. 537, 2005, pp. 349–385.

[19] Panda, J. and Seasholtz, R. G., "Experimental investigation of density fluctuations in high-speed jets and correlation with generated noise," *Journal of Fluid Mechanics*, Vol. 450, 2002, pp. 97–130.

[20] Sandberg, R., Sandham, N. D., and Suponitsky, V., "DNS of a fully turbulent jet flows in flight conditions including a canonical nozzle," *AIAA paper*, 2011.

[21] Guizar-Sicairos, M. and Gutiérrez-Vega, J. C., "Computation of quasi-discrete Hankel transforms of integer order for propagating optical wave fields," *Journal of the Optical Society of America A*, Vol. 21, No. 1, 2004, pp. 53–58.

[22] Sinayoko, S. and Agarwal, A., "On computing the physical sources of sound in a laminar jet," Submitted to *Journal of the Acoustical Society of America*.